JOURNAL OF COMPUTATIONAL PHYSICS 55, 485–514 (1984)

A Pseudospectral Algorithm for Three-Dimensional Magnetohydrodynamic Simulation

D. D. SCHNACK AND D. C. BAXTER

Applied Plasma Physics and Technology Division, Science Applications, Inc., La Jolla, California 92038

AND

E. J. CARAMANA

Los Alamos National Laboratory, Los Alamos, New Mexico 87545

Received October 7, 1983

An algorithm for the solution of the three-dimensional resistive magnetohydrodynamic equations in toroidal geometry is presented. The algorithm employs the pseudospectral method for approximation in the two periodic coordinates, and finite differences in the radial direction. Efficient Fast Fourier Transforms are used to communicate between configuration and Fourier space. Leapfrog time advancement is used for advective terms. Diffusion terms are treated implicitly to avoid severe time step restrictions. Sample cases are presented, and a comparison of the method with standard finite difference techniques is presented and discussed.

1. INTRODUCTION

It is now well established that multidimensional nonlinear resistive magnetohydrodynamics (MHD) is an excellent model for the description of the macroscopic dynamics of present magnetic fusion experiments. Two-dimensional simulation of these processes has become commonplace [1–3]. Such calculations have provided valuable insights into the interpretation of experimental diagnostics [4] and the nonlinear behavior of unstable modes in various devices [1, 5–7].

It has recently been recognized that two-dimensional motions, while enlightening, do not represent the true state of plasma dynamics, and that fully three-dimensional calculations are required [8, 9]. For tokamak plasmas, where one component of the magnetic field is everywhere large, it is possible to derive a reduced set of equations that adequately describes the dynamics of these devices [10]. Three-dimensional simulations of these equations have provided a detailed picture of plasma evolution [8, 9, 11]. These calculations can proceed much faster than solutions of the original

0021-9991/84 $3.00

equations. In other magnetic fusion devices, such as the spheromak and the reversed field pinch, no such generally applicable set of reduced equations exists at present, and one must solve the primitive equations. Incompressibility may provide some computational relief [12] but this assumption can only be justified a posteriori.

The periodic nature of the poloidal and toroidal directions in many fusion devices allows solutions to be represented by Fourier series in these coordinates. Simulations of tokamak plasmas with reduced equations have found that only a handful of these modes are important to the dynamics [13]. Codes developed for the solution of such problems have made use of this fact by introducing a mode selection process whereby only a few modes are retained in the calculation [14]. This procedure has also been used in incompressible simulations of the primitive equations [12]. The convolution sums that arise from the Fourier representation of quadratic nonlinearities in configuration space are then computed directly.

In fusion devices such as the reversed field pinch of the spheromak no a priori mode selection is possible. Indeed, there is reason to believe that many large-scale modes will be equally important [7]. Thus a large number of mode interactions are probable. These large-scale motions may serve to drive small-scale MHD turbulence, which may be responsible for such important physical effects as dynamo action and profile maintenance. Also, the particular path taken in the cascade of energy from long to short wavelength (along with the possibility of inverse cascades from short to long wavelength) is unknown and may be important. A large number (>100) of modes must therefore be retained in such calculations.

The physical and computational problems described above are similar to those encountered in the simulation of turbulent hydrodynamic flows. Accurate and efficient methods have been developed for the solution of these problems [15–20]. These spectral methods are based on the use of the Fast Fourier Transform (FFT), which allows the convolution sums to be evaluated in $O(N \ln_2 N)$ operations, as opposed to $O(N^2)$ operations for direct summation [15]. This allows many modes to be used in the simulation.

In this paper we describe an algorithm for the numerical solution of the primitive resistive MHD equations by these spectral methods, and present some examples of the application of the code based on this algorithm to the dynamics of magnetic fusion experiments. In Section 2 we present the mathematical model, and the coordinate system in which the model is applied. In Section 3 we discuss techniques of spatial approximation, including some details of the spectral and pseudospectral representations. The discussions here are by no means complete or rigorous, and are included to make the presentation self-contained. These methods have been described in great detail elsewhere [20]. In Section 4 we discuss methods of time advancement, including splitting of the spatial operators and time step restrictions. Section 5 contains examples of several types of computations that have been performed, including a comparison of our algorithm with standard finite differences.

2. Mathematical Model

2.1. *Basic Equations*

The study of large-scale dynamics in fusion and astrophysical plasmas involves the description of motions that occur on long time scales. In these cases the plasma acts as an electrically conducting fluid whose motions are adequately described by the single-fluid resistive magnetohydrodynamic (MHD) equations (see, for example, Ref. [21] for assumptions necessary for the validity of the model). In a suitable nondimensional form, they are

$$\frac{\partial \mathbf{B}}{\partial t} = -\mathbf{v} \cdot \nabla \mathbf{B} + \mathbf{B} \cdot \nabla \mathbf{v} - \mathbf{B} \nabla \cdot \mathbf{v} + \eta_0 \nabla^2 \mathbf{B} - \nabla \eta_0 \times (\nabla \times \mathbf{B}), \tag{1a}$$

$$\frac{\partial \mathbf{v}}{\partial t} = -\mathbf{v} \cdot \nabla \mathbf{v} + \frac{1}{\rho} \mathbf{B} \cdot \nabla \mathbf{B} - \frac{1}{2\rho} \nabla (p + B^2), \tag{1b}$$

$$\frac{\partial \rho}{\partial t} = -\mathbf{v} \cdot \nabla \rho - \rho \nabla \cdot \mathbf{v}, \tag{1c}$$

$$\frac{\partial p}{\partial t} = -\mathbf{v} \cdot \nabla p - \gamma p \nabla \cdot \mathbf{v} + 2(\gamma - 1)\, \eta_0 (\nabla \times \mathbf{B})^2 - \frac{p}{\tau}, \tag{1d}$$

where $\mathbf{B}$ is the magnetic field measured in units of a characteristic field B_0, $\mathbf{v}$ is the velocity measured in units of the Alfvén velocity $v_A = B_0/\sqrt{4\pi\rho_0}$, ρ is the mass density measured in units of a characteristic density ρ_0, p is the thermodynamic pressure measured in units of $p_0 = B_0^2/8\pi$, γ is the ratio of specific heats, and all lengths are measured in units of a characteristic length a. The coefficient η_0 is a nondimensional resistivity that may be a function of the dependent variables. When the resistivity is constant in space and time, η_0 is the inverse of the Lundquist number $S = t_R/t_A$, where $t_R = 4\pi a^2/c^2\eta$ is the resistive diffusion time and $t_A = a/v_A$ is the Alfvén transit time. Note that S is defined in terms of the normalization constants, and is not to be confused with the magnetic Reynolds number R_M, which is defined in terms of local quantities. The last term in Eq. (1d) represents energy losses not directly encompassed by the model, and is included to control the effects of Joule heating on plasma beta ($\beta \equiv 8\pi p/B^2$).

When η_0 vanishes, Eq. (1a)–(1d) define the ideal MHD model. A finite value of η_0 relaxes the flux topology constraints of these equations with the result that previously unallowed motions are possible [22]. These new dynamical processes are essential for an adequate description of fusion and astrophysical plasmas. The inclusion of further dissipative processes, such as ion viscosity of thermal conduction, removes no further constraints on the magnetic topology. In extremely hot or strongly magnetized plasmas these transport coefficients become highly anisotropic, with values parallel to the local magnetic field lines far exceeding those in the perpendicular directions. In

these cases (when the parallel mean free path becomes comparable to macroscopic scale lengths) it is not clear that first-order transport theory is an adequate description of parallel transport. We thus exclude these effects from the model.

We note that the compressible nature of Eqs. (1a)–(1d) admits the propagation of Alfvén (fast magnetosonic) waves perpendicular to the field. These waves evolve on a time scale defined by a cross-field scale length divided by the Alfvén velocity. For a diffuse pinch this length scale is the minor radius. Since many phenomena of interest occur on much longer times scales, this presents a computational problem. In some fusion experiments (such as the tokamak) one component of the magnetic field is everywhere large. This allows a self-consistent ordering in which the plasma becomes incompressible, and the magnetosonic wave is eliminated [10]. The remaining high-frequency normal mode is the shear Alfvén wave propagating parallel to the field. This wave evolves on a time scale defined by a parallel scale length divided by the Alfvén velocity. In fusion experiments in which the incompressible ordering is valid, this scale length is the major radius. Thus in these cases the fast time scale is increased by a factor that is of the order of the aspect ratio, thereby greatly reducing the computational requirements. However, in general such orderings are not possible, and there is no a priori justification for eliminating compressibility from the model. Indeed, for highly sheared, low-q devices such as the reversed field pinch a shear Alfvén wave travelling near the field reversal surface evolves on a time scale that is on the order of the minor radius divided by the Alfvén velocity, i.e., the same order as that of the compressible wave. Such effects may be minimized in incompressible calculations by choosing a relatively coarse poloidal mesh [12], but such real physics effects as Ohmic heating, adiabatic compression, and density fluctuations are then missed. Thus to make the maximum contact with experimental fusion plasmas in a wide variety of configurations we retain compressibility in our model.

2.2. Coordinate System

We choose to express Eqs. (1a)–(1d) in the (r, θ, ζ) coordinate system shown in Fig. 1, where $0 \leqslant r \leqslant a$, $0 < \theta \leqslant 2\pi$, $0 \leqslant \zeta \leqslant 2\pi$. This system describes a circular cross section of radius a rotated through 2π radians about an axis (the major axis) a distance R_0 from the center of the circle. The path traced by the center of the circle during a rotation through the angle ζ is called the minor axis. The coordinate system is related to cylindrical coordinates (R, ϕ, Z) referred to the major axis by

$$R = R_0 + r \cos \theta, \tag{2a}$$

$$Z = r \sin \theta, \tag{2b}$$

$$\phi = -\zeta, \tag{2c}$$

and is suitable for the description of confined toroidal plasma systems with circular cross section.

The vector differential operators appearing on the righ-hand side of Eqs. (1a)–(1d)

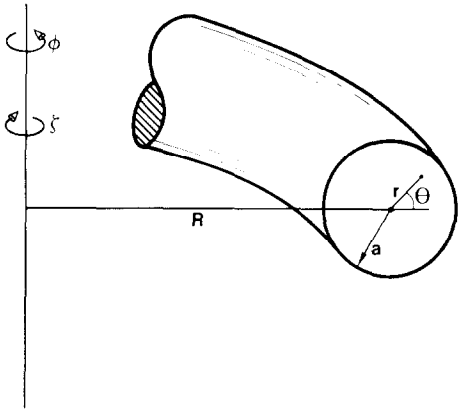

FIG. 1. Coordinate system.

can be expressed in this coordinate system by using the curvilinear coordinate scale factors

$$h_r = 1, \tag{3a}$$

$$h_\theta = r, \tag{3b}$$

$$h_\zeta \equiv \tau^{-1} = (1 + \alpha\varepsilon r \cos\theta)/\varepsilon, \tag{3c}$$

where $\varepsilon = a/R_0$ is the inverse aspect ratio of the torus. When $\alpha = 1$ the coordinate system is as described above. Setting $\alpha = 0$ allows reduction to cylindrical coordinates $(r, \theta, z = \zeta/\varepsilon)$ referred to the minor axis.

After some algebra, the resistive MHD equations then become

$$\begin{aligned}
\frac{\partial B_r}{\partial r} = &-v_r \frac{\partial B_r}{\partial r} + B_r \frac{\partial v_r}{\partial r} - \frac{B_r}{r}\frac{\partial}{\partial r}(r v_r) - \frac{v_\theta}{r}\frac{\partial B_r}{\partial \theta} \\
&+ \frac{B_\theta}{r}\frac{\partial v_r}{\partial \theta} - \frac{B_r}{r}\frac{\partial v_\theta}{\partial \theta} - \tau\left(v_\zeta \frac{\partial B_r}{\partial \zeta} - B_\zeta \frac{\partial v_r}{\partial \zeta} + B_r \frac{\partial v_\zeta}{\partial \zeta}\right) \\
&- \alpha\tau B_r(v_r \cos\theta - v_\theta \sin\theta) \\
&+ \eta_0 \left\{ \frac{1}{r}\frac{\partial}{\partial r}\left(r\frac{\partial B_r}{\partial r}\right) + \frac{1}{r^2}\frac{\partial^2 B_r}{\partial \theta^2} + \tau^2 \frac{\partial^2 B_r}{\partial \zeta^2} \right. \\
&- \frac{B_r}{r^2} - \frac{2}{r^2}\frac{\partial B_\theta}{\partial \theta} + \alpha\tau\left[\cos\theta\left(\frac{\partial B_r}{\partial r} - 2\tau\frac{\partial B_\zeta}{\partial \zeta}\right)\right. \\
&\left.\left. - \frac{\sin\theta}{r}\left(\frac{\partial B_r}{\partial \theta} - B_\theta\right) - \tau\cos\theta(B_r\cos\theta - B_\theta \sin\theta)\right]\right\},
\end{aligned} \tag{4a}$$

$$\frac{\partial B_\theta}{\partial t} = -v_r \frac{\partial B_\theta}{\partial r} + B_r \frac{\partial v_\theta}{\partial r} + \frac{B_\theta v_r - B_r v_\theta}{r} - \frac{B_\theta}{r}\frac{\partial}{\partial r}(r v_r) - \frac{v_\theta}{r}\frac{\partial B_\theta}{\partial \theta}$$
$$- \tau\left(v_\zeta \frac{\partial B_\theta}{\partial \zeta} - B_\zeta \frac{\partial v_\theta}{\partial \zeta} + B_\theta \frac{\partial v_\zeta}{\partial \zeta}\right) - \alpha\tau B_\theta (v_r \cos\theta - v_\theta \sin\theta)$$
$$+ \eta_0 \left\{ \frac{1}{r}\frac{\partial}{\partial r}\left(r \frac{\partial B_\theta}{\partial r}\right) + \frac{1}{r^2}\frac{\partial^2 B_\theta}{\partial \theta^2} + \tau^2 \frac{\partial^2 B_\theta}{\partial \zeta^2} - \frac{B_\theta}{r^2} + \frac{2}{r^2}\frac{\partial B_r}{\partial \theta} \right.$$
$$+ \alpha\tau \left[\cos\theta \frac{\partial B_\theta}{\partial r} - \frac{\sin\theta}{r}\left(\frac{\partial B_\theta}{\partial \theta} + B_r - 2\tau \frac{\partial B_\zeta}{\partial \zeta}\right)\right.$$
$$\left.\left. + \tau \sin\theta (B_r \cos\theta - B_\theta \sin\theta)\right]\right\} - \frac{d\eta_0}{dr}\left[\frac{1}{r}\frac{\partial}{\partial r}(r B_\theta) - \frac{1}{r}\frac{\partial B_r}{\partial \theta}\right], \tag{4b}$$

$$\frac{\partial B_\zeta}{\partial t} = - v_r \frac{\partial B_\zeta}{\partial r} + B_r \frac{\partial v_\zeta}{\partial r} - \frac{B_\zeta}{r}\frac{\partial}{\partial r}(r v_r) - \frac{v_\theta}{r}\frac{\partial B_\zeta}{\partial \theta}$$
$$+ \frac{B_\theta}{r}\frac{\partial v_\zeta}{\partial \theta} - \frac{B_\zeta}{r}\frac{\partial v_\theta}{\partial \theta} - \tau v_\zeta \frac{\partial B_\zeta}{\partial \zeta} - \alpha\tau v_\zeta (B_r \cos\theta - B_\theta \sin\theta)$$
$$+ \eta_0 \left\{ \frac{1}{r}\frac{\partial}{\partial r}\left(r \frac{\partial B_\zeta}{\partial r}\right) + \frac{1}{r^2}\frac{\partial^2 B_\zeta}{\partial \theta^2} + \tau^2 \frac{\partial^2 B_\zeta}{\partial \zeta^2} \right.$$
$$+ \alpha\tau \left[\cos\theta \frac{\partial B_\zeta}{\partial r} - \frac{\sin\theta}{r}\frac{\partial B_\zeta}{\partial \theta} - \tau B_\zeta \right.$$
$$\left.\left. + 2\tau \left(\cos\theta \frac{\partial B_r}{\partial \zeta} - \sin\theta \frac{\partial B_\theta}{\partial \zeta}\right)\right]\right\}$$
$$+ \frac{d\eta_0}{dr}\left[\tau \frac{\partial B_r}{\partial \zeta} - \frac{\partial B_z}{\partial r} - \alpha\tau B_\zeta \cos\theta\right], \tag{4c}$$

$$\frac{\partial v_r}{\partial t} = - v_r \frac{\partial v_r}{\partial r} + \frac{B_r}{\rho}\frac{\partial B_r}{\partial r} - \frac{v_\theta}{r}\frac{\partial v_r}{\partial \theta} + \frac{B_\theta}{\rho}\frac{1}{r}\frac{\partial B_r}{\partial \theta}$$
$$- \tau\left(v_\zeta \frac{\partial v_r}{\partial \zeta} - \frac{B_\zeta}{\rho}\frac{\partial B_r}{\partial \zeta}\right) + \frac{v_\theta^2 - B_\theta^2/\rho}{r} - \frac{1}{2\rho}\frac{\partial}{\partial r}(p + B^2)$$
$$+ \alpha\tau \cos\theta (v_\zeta^2 - B_\zeta^2/\rho), \tag{4d}$$

$$\frac{\partial v_\theta}{\partial t} = - v_r \frac{\partial v_\theta}{\partial r} + \frac{B_r}{\rho}\frac{\partial B_\theta}{\partial r} - \frac{v_\theta}{r}\frac{\partial v_\theta}{\partial \theta} + \frac{B_\theta}{\rho}\frac{1}{r}\frac{\partial B_\theta}{\partial \theta}$$
$$- \tau\left(v_\zeta \frac{\partial v_\theta}{\partial \zeta} - \frac{B_\zeta}{\rho}\frac{\partial B_\theta}{\partial \zeta}\right) - \frac{v_\theta^2 - B_r B_\theta/\rho}{r} - \frac{1}{2\rho}\frac{1}{r}\frac{\partial}{\partial \theta}(p + B^2)$$
$$- \alpha\tau \sin\theta (v_\zeta^2 - B_\zeta^2/\rho), \tag{4e}$$

$$\frac{\partial v_\zeta}{\partial t} = -v_r \frac{\partial v_\zeta}{\partial r} + \frac{\partial B_\zeta}{\partial r} - \frac{v_\theta}{r}\frac{\partial v_\zeta}{\partial \theta} + \frac{B_\theta}{\rho}\frac{1}{r}\frac{\partial B_\theta}{\partial \theta}$$
$$- \tau\left(v_\zeta \frac{\partial v_\zeta}{\partial \zeta} - \frac{B_\zeta}{\rho}\frac{\partial B_\zeta}{\partial \zeta}\right) - \frac{1}{2\rho}\tau\frac{\partial}{\partial \zeta}(p + B^2)$$
$$- \alpha\tau\left[v_\zeta(v_r \cos\theta - v_\theta \sin\theta) - \frac{B_\zeta}{\rho}(B_r \cos\theta - B_\theta \sin\theta)\right], \tag{4f}$$

$$\frac{\partial \rho}{\partial t} = -v_r \frac{\partial \rho}{\partial r} - \frac{\rho}{r}\frac{\partial}{\partial r}(r v_r) - \frac{v_\theta}{r}\frac{\partial \rho}{\partial \theta} - \frac{\rho}{r}\frac{\partial v_\theta}{\partial \theta}$$
$$-\tau\left(v_\theta \frac{\partial \rho}{\partial \zeta} + \rho\frac{\partial v_\zeta}{\partial \zeta}\right) + \alpha\tau\rho(v_r \cos\theta - v_\theta \sin\theta), \tag{4g}$$

$$\frac{\partial p}{\partial t} = -v_r \frac{\partial p}{\partial r} - \gamma p \frac{1}{r}\frac{\partial}{\partial r}(r v_r) - \frac{v_\theta}{r}\frac{\partial p}{\partial \theta} - \gamma p \frac{1}{r}\frac{\partial v_\theta}{\partial \theta}$$
$$- \tau\left(v_\zeta \frac{\partial p}{\partial \zeta} + \gamma p \frac{\partial v_\zeta}{\partial \zeta}\right) - \alpha\gamma p\tau(v_r \cos\theta - v_\theta \sin\theta)$$
$$+ 2(\gamma - 1)\eta_0 \left\{\left[\frac{1}{r}\frac{\partial B_\zeta}{\partial \theta} - \tau\left(\frac{\partial B_\theta}{\partial \zeta} + B_\zeta \sin\theta\right)\right]^2\right.$$
$$\left. + \left[\frac{\partial B_\zeta}{\partial r} - \tau\left(\frac{\partial B_r}{\partial \zeta} - B_\zeta \cos\theta\right)\right]^2 + \left[\frac{1}{r}\frac{\partial}{\partial r}(r B_\theta) - \frac{1}{r}\frac{\partial B_r}{\partial \theta}\right]^2\right\}. \tag{4h}$$

Note that, for reasons to be discussed in Section 4, we have assumed $\eta_0 = \eta_0(r)$. Equations (4a)–(4h) comprise eight equations in the eight primitive variables (B_r, B_θ, B_ζ, v_r, v_θ, v_ζ, ρ, p), and are the equations that we solve numerically. (In practice, only two of Eqs. (4a)–(4c) are advanced in time; the remaining component of $\mathbf{B}$ is determined from the condition $\nabla \cdot \mathbf{B} = 0$, thus assuring that the fields remain solenoidal.)

3. Spatial Approximation

In the numerical solution of Eqs. (4a)–(4h) the state variable $\mathbf{U} = (B_r, B_\theta, B_\zeta, v_r, v_\theta, v_\zeta, \rho, p)$ is represented on mesh of $N_r \times N_\theta \times N_\zeta$ grid points (r_i, $i = 1, N_r$; θ_j, $j = 1, N_\theta$; ζ_k, $k = 1, N_\zeta$). The spacing in the poloidal (θ) and toroidal (ζ) directions is uniform such that $\Delta\theta = 2\pi/N_\theta$, $\Delta\zeta = 2\pi/N_\zeta$. We allow for nonuniform mesh spacing in the radial coordinate, but in practice a uniform spacing $\Delta r = a/(N_r - 1)$ is used, for reasons to be discussed later.

The periodic nature of the solution vector $\mathbf{U}$ with respect to the θ and ζ coordinates allows a spectral representation to be employed for the finite approximation of spatial

operators in these directions, since this representation is uniformly convergent at the boundaries 0 and 2π. The radial coordinate is treated by the method of finite differences. These methods are discussed in more detail in the following sections.

3.1. *Spectral Representation for the Periodic Coordinates*

It is possible to represent any function on the interval ($0 \leqslant \theta \leqslant 2\pi$, $0 \leqslant \zeta \leqslant 2\pi$) by the complex Fourier series,

$$u(\theta, \zeta, t) = \sum_{m=-\infty}^{\infty} \sum_{n=-\infty}^{\infty} a_{m,n}(t)\, e^{i(m\theta + n\zeta)}, \tag{5}$$

where the complex Fourier coefficients are given by

$$a_{m,n}(t) = \int_0^{2\pi} \frac{d\theta}{2\pi} \int_0^{2\pi} \frac{d\zeta}{2\pi}\, u(\theta, \zeta, t)\, e^{-i(m\theta + n\zeta)}. \tag{6}$$

The reality of $u(\theta, \zeta)$ requires that

$$a_{m,n} = a^*_{-m,-n}, \tag{7}$$

where $(\,)^*$ represents complex conjugation.

When the function $u(\theta, \zeta)$ is approximated by $M \times N$ data points e.g., stored on a mesh), it can be represented by the finite Fourier series

$$u_{MN}(\theta_j, \zeta_k, t) = \sum_{n=-M/2+1}^{M/2} \sum_{n=-N/2+1}^{N/2} a_{m,n}(t)\, e^{i(m\theta_j + n\zeta_k)}, \tag{8}$$

with

$$a_{m,n}(t) = \frac{1}{MN} \sum_{j=1}^{M} \sum_{k=1}^{N} u_{MN}(\theta_j \zeta_k, t)\, e^{-i(m\theta_j + n\zeta_k)}. \tag{9}$$

Here $u_{MN}(\theta_j, \zeta_k, t)$ is the MN-term approximation to the function $u(\theta, \zeta, t)$ evaluated at the mesh point (θ_j, ζ_k) at time t; $\theta_j = (j-1)\, 2\pi/M$ and $\zeta_k = (k-1)\, 2\pi/N$. The derivatives $\partial u/\partial\theta$ and $\partial u/\partial\zeta$ at the point (θ_j, ζ_k) and time t are given by

$$\left(\frac{\partial u_{MN}}{\partial \theta}\right)_{j,k} = \sum_{m=-M/2+1}^{M/2} \sum_{n=-N/2+1}^{N/2} ima_{m,n}(t)\, e^{i(m\theta_j + n\zeta_k)}, \tag{10a}$$

$$\left(\frac{\partial u_{MN}}{\partial \zeta}\right)_{j,k} = \sum_{m=-M/2+1}^{M/2} \sum_{n=-N/2+1}^{N/2} ina_{m,n}(t)\, e^{i(m\theta_j + n\zeta_k)}. \tag{10b}$$

The spectral representation of the equations of motion is obtained by employing Eqs. (8) and (10) in some appropriate manner (to be discussed in Section 3.2) in the right-hand side of the Eq. (4a)–(4h). This technique has several distinct advantages

over finite difference methods. These properties are well documented [20], and are discussed here only briefly.

3.1.1. *Phase Error*

To illustrate the phase error in finite difference representations, consider the model differential equation

$$\frac{\partial u}{\partial t} = c\frac{\partial u}{\partial x}, \qquad 0 \leqslant x \leqslant 2\pi, \quad u(0, t) = u(2\pi, t). \tag{11}$$

Using the one-dimensional analogue of Eq. (5), we obtain a set of differential equations for the Fourier coefficients

$$\frac{da_n}{dt} = icna_n, \qquad -\infty \leqslant n \leqslant \infty. \tag{12}$$

Now represent Eq. (11) on a set of N mesh points x_j, where $x_j = (j-1)\,2\pi/N$. If we employ the second-order finite difference approximation to the spatial derivative

$$\left(\frac{\partial u}{\partial x}\right)_j = \frac{u_{j+1} - u_{j-1}}{2\Delta x}, \qquad j = 2, 3, \ldots, N-1. \tag{13}$$

and make use of the one-dimensional analogue of Eq. (8), we find that in this representation the Fourier coefficients evolve according to the N equations

$$\frac{da_n}{dt} = ic\left(\frac{\sin n\Delta x}{\Delta x}\right)a_n, \qquad -\frac{N}{2} + 1 \leqslant n \leqslant \frac{N}{2}. \tag{14}$$

Thus Eq. (13) accurately approximates the solution of Eq. (11) only for long-wavelength ($|n| \ll N/2$) modes. This representation is dispersive, with different wavelengths propagating at different velocities. Phase error of this type is inherent in all finite difference approximations to Eq. (11).

Now consider Eq. (10), the spectral representation of the derivative. When this and Eq. (8) are employed, Eq. (11) becomes the set of N equations

$$\frac{da_n}{dt} = icna_n, \qquad -\frac{N}{2} + 1 \leqslant n \leqslant \frac{N}{2}, \tag{15}$$

which is identical with the exact Eq. (12) except for the finite number of modes. Thus all modes retained in the representation (8) satisfy the exact dispersion relation. The only error is due to the retention of a finite number of terms in the Fourier series. This truncation error is discussed in the next section.

3.1.2. *Convergence: Order of Accuracy*

In the previous section we showed that the spectral representation (8) and (10) leads to a faithful reproduction of the phase properties of all modes retained. Here we consider the error after N terms in approximating the solution of Eq. (11).

For any $t > 0$, we consider the error [20]

$$\varepsilon_N(t) = u(x, t) - u_N(x, t). \tag{16}$$

For large N, we have $|\varepsilon_N| \sim |a_N|$. Integrating the one-dimensional analogue of Eq. (6) by parts p times, assuming that $u(x)$ has continuous derivatives up to order $p-1$, and that $u^{(p)}(x)$ is integrable, it can be shown that

$$|a_N| \ll 1/N^p, \qquad N \to \infty. \tag{17}$$

In particular, if $u(x)$ is infinitely differentiable and periodic on $0 \leqslant x \leqslant 2\pi$, then the error ε_N goes to zero faster than any power of $1/N$ as $N \to \infty$. This is to be contrasted with pth-order-accurate finite difference methods wherein the error vanishes like $1/N^p$. (Equivalent accuracy is obtained in spectral methods for functions that are $p-1$ times differentiable.) Thus spectral methods require relatively fewer modes (mesh points) to obtain the same accuracy as a given finite difference method.

As with finite differences, the analysis in this and the previous section strictly holds only for linear equations. However, there is a great body of evidence that indicates that these properties continue to hold when nonlinearities are considered [20]. Spectral methods are, however, subject to aliasing errors. These are discussed in Section 3.2.1.

3.1.3. *Computation Time*

The evaluation of the finite difference approximation to the first derivative, Eq. (13), for all mesh points x_j requires $O(N)$ operations. The direct evaluation of the spectral series, Eq. (10), for all mesh points x_j requires $\sim O(N^2)$ operations. Similar scalings hold for the direct evaluation of quadratic nonlinearities and convolution sums. However, when Fast Fourier Transforms (FFTs) are used [23], the evaluation of finite Fourier series and convolution sums can be reduced to $\sim O(N \ln_2 N)$ operations [15]. Such methods are called pseudospectral, and are discussed in the next section. They require computer time comparable with finite difference methods of the same resolution. In practice they are somewhat slower. However, because of the exponential convergence properties discussed in Section 3.1.2, they require less computer time than finite difference methods of the same accuracy. Examples of this are shown in Section 5.4.

3.2. *The Pseudo-Spectral Method*

Consider the equation

$$\frac{\partial u}{\partial t} = u \frac{\partial u}{\partial x} + \eta \frac{\partial^2 u}{\partial x^2} + f, \qquad 0 \leqslant x \leqslant 2\pi, \tag{18a}$$

$$u(0, t) = u(2\pi, t), \tag{18b}$$

$$f(0, t) = f(2\pi, t), \tag{18c}$$

which contains the essential features of the resistive MHD Eqs. (4a)–(4h). The first term on the right-hand side represents the quadratic nonlinearity introduced by the convective derivative, the second term models the effects of dissipation, and the third term represents sources, sinks, lower-order linear terms, forcing functions, etc. Here we will consider only the approximations to the first and third terms. The dissipation term is discussed in Section 4.3.

Substituting (8) and (10) into (18), taking the inner product with $\exp(-ipx)$, and ignoring the dissipative term, we arrive at a set of evolutionary equations for the N Fourier coefficients a_p:

$$\frac{da_p}{dt} = -i \sum_{n=-N/2+1}^{N/2} (p-n)\, a_n a_{p-n} + f_p, \qquad p = 0, 1, \ldots, \frac{N}{2}, \tag{19a}$$

$$a_{-p} = a_p^*. \tag{19b}$$

The set (19) is the spectral representation of Eq. (18). As mentioned in Section 3.1.3, the direct evaluation of Eq. (19) for all a_p requires $O(N^2)$ operations, as compared to $O(N)$ operations for finite differences. Additionally, while completely accurate, Eq. (19) suffers from the defect that it can be quite complicated (especially when applied to the full resistive MHD equations), and that it does not have the familiar form of the configuration space Eq. (18). We are thus led to the pseudospectral method, in which both the form of the original equation and the desirable properties of the spectral representation are retained.

The pseudospectral approximation takes advantage of the fact that multiplication is most efficiently performed in configuration space and differentiation is most accurately performed in Fourier space. Fast Fourier Transforms are used to communicate between the two representations. In principle it is irrelevant whether the dependent variables are the N Fourier coefficients, as in Eq. (19), or the values of $u(x_j)$ stored at the N mesh points x_j in configuration space. In the first case the transformation is made to configuration space to perform the convolution; in the second case the transformation is made to Fourier space to perform the differentiation. Both methods have the same accuracy, i.e., those of the fully spectral methods described previously. Because of its familiarity, we have chosen the configuration space representation.

The configuration space pseudospectral approximation to Eq. (18) at mesh point x_j is

$$\left(\frac{\partial u_N}{\partial t}\right)_j = -u_N(x_j)\left(\frac{\partial u_N}{\partial x}\right)_j + f_N(x_j), \qquad j = 1, 2, \ldots, N, \tag{20}$$

where $(\partial u_N/\partial x)_j$ is evaluated as in Eq. (10). The function $u_N(x_j)$ is stored on the mesh x_j in configuration (physical) space. The array $(\partial u_N/\partial x)_j$ is generated by

transforming to Fourier space [Eq. (9)] to obtain the a_n, and then transforming the array ina_n back to configuration space [Eq. (10)]. The quadratic nonlinearity is then evaluated as a multiplication of the arrays $u_N(x_j)$ and $(\partial u_N/\partial x)_j$ at each x_j.

When FFTs are used, evaluation of Eq. (20) at all mesh points requires $O(N \ln_2 N)$ operations. Thus, as mentioned in Section 3.1.4, the pseudospectral method is comparable in speed to finite difference with the same spatial resolution.

It is to be emphasized that a by-product of pseudospectral method is the simplicity of the resulting equations. Both the function and its derivative appear as arrays, the latter being readily evaluated by a single subroutine call. The coding closely resembles the equation being solved, making debugging a relatively easy task resulting in reduced code development time.

3.2.1. *Aliasing Errors*

We have shown in Section 3.1 that spectral methods can lead to a physically realistic and rapidly convergent approximation to a linear equation. When nonlinearities are present, as in Eq. (18a), these methods are subject to aliasing errors [15, 17, 18, 20] that arise from the generation by quadratic nonlinearities of modes with wavelength shorter than $\pi/\Delta x$. These errors, and an algorithm for preventing them, are discussed below.

Consider two variables u_j and v_j, defined on a set of N mesh points $x_j = 2\pi j/N$, and their Fourier coefficients a_k, b_k. Then

$$u_j = \sum_{k=-N/2+1}^{N/2}{}' a_k e^{i2\pi jk/N}, \tag{21a}$$

$$v_j = \sum_{k=-N/2+1}^{N/2}{}' b_k e^{i2\pi jk/N}, \tag{21b}$$

and

$$a_k = \frac{1}{N} \sum_{j=0}^{N-1}{}' u_j e^{-i2\pi jk/N}, \tag{22a}$$

$$b_k = \frac{1}{N} \sum_{j=0}^{N-1}{}' v_j e^{-i2\pi jk/N}. \tag{22b}$$

The product $w_j = u_j v_j$ has the Fourier expansion

$$w_j = \sum_{l=-N/2+1}^{N/2}{}' c_l e^{i2\pi jl/N},$$

$$c_l = \frac{1}{N} \sum_{j=0}^{N-1}{}' w_j e^{-i2\pi jl/N},$$

with the c_l's are related to a_k, b_k by

$$c_l = \sum_{k=-N/2+1}^{N/2} a_k b_{l-k}, \qquad -\frac{N}{2}+1 \leqslant l \leqslant \frac{N}{2}. \tag{23}$$

Note that the range of the index $k' \equiv l-k$ in Eq. (23) is $-N+1 \leqslant k' \leqslant N-1$, which is outside the range employed in Eqs. (21a)–(21b). Thus the c_l's will contain information from modes that are not resolved in the original representation. We now discuss the nature of this error.

Even though Eqs. (22a)–(22b) define coefficients of the finite Fourier series (21a)–(21b) only for $-N/2+1 \leqslant k \leqslant N/2$, they remain valid function definitions for values of k outside this range. In fact, evaluating Eq. (22b) for $k' \equiv l-k = N-k_0 > N/2$ we find that the coefficient b_{l-k} in Eq. (23) (that is *not* defined in the original representation) has the same value as b_{l-k-N} (that *is* a proper Fourier coefficient). Similarly, when $l-k < -(N/2)+1$, b_{l-k} appears as b_{l-k+N}. This phenomenon of one mode appearing as another is called aliasing error. We have found that such errors can lead to nonlinear instabilities after many time steps.

Aliasing errors can be prevented in pseudospectral methods by removing the

in Eqs. (21) and (23) to range over $-M \leqslant l \leqslant M$, $-M \leqslant k \leqslant M$ such that $l-k-N < -M$ and $l-k+N > M$. Modes outside this range are set to zero, since it is these terms that contain the aliasing errors. Applying these conditions we find

$$M < N/3. \tag{24}$$

Since $k_{\max} = N/2$, aliasing errors are prevented by using two-thirds of available Fourier space.

3.3. *Representation of the Radial Coordinate*

Since the solutions of Eqs. (4a)–(4h) are not periodic in the radial coordinate r, the techniques discussed in Sections 3.2 and 3.3 are not directly applicable. Similar problems are encountered in viscous hydrodynamic problems in nonperiodic domains, such as flow in pipes or rectangular channels. In these cases approximation in the nonperiodic coordinate is accomplished by expansion in Chebyshev polynomials [20], which have the desirable property that their zeros (collocation points) are densely spaced near the outer boundary giving a naturally concentrated mesh there. This is important since hydrodynamic boundary layers form in this region. In resistive MHD, the important boundary layers are associated with filamentation of current, occur internally, and may form spontaneously at non-predetermined locations. Thus a uniform mesh, or one that is internally dense, is desirable. Expansion in Bessel functions, the natural functions for analytic investigation, is flawed by nonuniform convergence at the outer boundary and lack of a fast transform algorithm [20]. Thus, in spite of the deficiencies discussed in Section 3.1, we choose finite differences as the most efficient representation of the radial coordinate.

We define the following approximation to the first and second radial derivatives appearing in Eqs. (4a) – (4h):

$$u\frac{\partial u}{\partial r} = u_i \frac{u_{i+1} - u_{i-1}}{\Delta_+ r_i + \Delta_- r_i}; \tag{25a}$$

$$\frac{1}{r}\frac{\partial}{\partial r}(ru) = 2\frac{r_{i+1/2}u_{i+1/2} - r_{i-1/2}u_{i-1/2}}{r_i(\Delta_+ r_i + \Delta_- r_i)}; \tag{25b}$$

$$\frac{1}{r}\frac{\partial}{\partial r}\left(r\frac{\partial u}{\partial r}\right) = \frac{2}{r_i(\Delta_+ r_i + \Delta_- r_i)}\left[r_{i+1/2}\left(\frac{u_{i+1} - u_i}{\Delta_+ r_i}\right) - r_{i-1/2}\left(\frac{u_i - u_{i-1}}{\Delta_- r_i}\right)\right]; \tag{25c}$$

where $\Delta_+ r_i = r_{i+1} - r_i$, $\Delta_- r_i = r_i - r_{i-1}$, and $r_{i\pm 1/2} = (r_{i\pm 1} + r_i)/2$. While we have allowed for a nonuniform radial mesh, in practice a uniform mesh employed, as discussed above. On this mesh, Eqs. (25a)–(25c) attain second-order accuracy.

Note that we use the centered difference formula, Eq. (25a), rather than donor cell, or upstrem–downstream, methods. When the latter methods are applied to toroidal locations differing in phase by π/n radians [so that for the nth mode $u_n(r, \theta, \zeta) = -u_n(r, \theta, \zeta + \pi/n)$] the implied relationship $\partial u_n(r, \theta, \zeta)/\partial r = -\partial u_n(r, \theta, \zeta + \pi/n)/\partial r$ is not retained, due to the change in sign of u_n. We have found this to cause anomalous rotation of the plasma column.

3.4. *Radial Smoothing*

In Section 3.1.1 we discussed the inherent inaccuracies in the representation of short-wavelength modes with finite difference methods. These phase errors, coupled with the natural tendency of the quadratic nonlinearities to propagate information to short wavelengths, can lead to an accumulation of short-wavelength noise that, while not necessarily unstable, may eventually dominate the solution.

In our algorithm, this noise appears only in the radial direction. We remove it by applying a spatial filter that damps the short-wavelength modes while leaving the longer wavelengths relatively unchanged. After the solution has been advanced a complete time step by the methods discussed in Section 4, it is modified at each point by

$$u_{ijk}^{n+1} = u_{ijk}^* + \alpha(u_{i+1,j,k}^* - 2u_{i,j,k}^* + u_{i-1,j,k}^*), \tag{26}$$

where u^* is the latest approximation to u^{n+1}, obtained by time advancement, and $0 \leqslant \alpha \leqslant \frac{1}{4}$. When $\alpha = \frac{1}{4}$, the amplitude of the $k_0 = \pi/\Delta r$ mode is reduced to zero, while that of the $k = \pi/5\Delta r$ ($\lambda = 10\Delta r$) mode is reduced by less than 10%. In practice we use either $\alpha = \frac{1}{8}$ or $\alpha = \frac{1}{4}$.

The smoothing algorithm (26) is equivalent to adding a term of the form $\sigma\partial^2 u/\partial r^2$ to the equations, where $\sigma = \alpha\Delta r^2/\Delta t$. The scheme is this stable for $\alpha < \frac{1}{2}$, as is always the case.

3.5. *Boundary Conditions*

To obtain a solution, Eqs. (1a)–(1d) must be supplemented by boundary conditions. Periodicity is automatically obtained in the θ and ζ coordinates. We assume that the surrounding circular cross-section wall is nonporous, and is a good electrical conductor. Thus

$$\hat{n} \cdot \mathbf{v} = 0, \tag{27a}$$

$$\hat{n} \cdot \mathbf{B} = 0, \tag{27b}$$

at $r = a$, where $\hat{n}$ is a unit vector normal to the wall. Evolutionary equations for the tangential components of $\mathbf{v}$ at the wall are found by employing (27a)–(27b) in Eq. (1b). The result is

$$\frac{\partial \mathbf{v}_t}{\partial t} = \mathbf{v}_t \cdot \nabla_t \mathbf{v} + \hat{n}\hat{n} \cdot (\mathbf{v}_t \cdot \nabla_t \mathbf{v}) - \frac{1}{\rho} \nabla_t p$$

$$- \frac{1}{\rho} (\mathbf{B} \times \hat{n}) \mathbf{J} \cdot \hat{n}, \tag{28}$$

where $\mathbf{v}_t = (\hat{n} \times \mathbf{v}) \times \hat{n}$ is the tangential component of $\mathbf{v}$, and operator ∇_t is defined through the relationship

$$\nabla \equiv \hat{n}\hat{n} \cdot \nabla + \nabla_t. \tag{29}$$

When the wall is perfect electrical conductor, we have the condition

$$\hat{n} \times \mathbf{J} = 0, \tag{30}$$

which may be used to derive boundary conditions on the normal derivatives of $\mathbf{B}_t$. However, we have found it superior to use Eq. (30) and (27a)–(27b) in Eq. (1a) to derive evolutionary equations similar to (28) for the tangential components of $\mathbf{B}$. In many applications, magnetic flux may enter or leave through the wall (e.g., from an external electrical circuit). In this case the wall does not appear as a perfect conductor to the mean fields, and separate conditions on these Fourier components are employed.

It remains to specify boundary conditions on the thermodynamic quantities p and ρ. An evolutionary equation for the density is obtained by employing (27a) in (1c), while evaluating the normal component of (1b) at the wall yields

$$\hat{n} \cdot \nabla p = -\hat{n} \cdot (\rho \mathbf{v} \cdot \nabla \mathbf{v} - \mathbf{J} \times \mathbf{B}) \tag{31}$$

as a condition on the normal derivative of the pressure.

In addition to the physical boundary at the wall enumerated above, conditions must be imposed at the origin $r = 0$. These may be derived by requiring the solution to be analytic independent of numerical approximation. Similar ideas have been

discussed in detail elsewhere [3]. Scalar quantities $(B_\zeta, V_\zeta, \rho, p)$ can have only finite $m=0$ Fourier amplitudes, and vector components $(B_r, B_\theta, v_r, v_\theta)$ can have only finite $m=1$ Fourier amplitudes at the origin that are related by $B_\theta = iB_r$, $v_\theta = iv_r$. The Taylor series expansion of these quantities about the origin consists of only even powers of r. The $m=1$ components of scalar quantities and the $m=0$ components of vector quantities have a power series about the origin that consists of only odd powers of r. (This can be shown by induction since the gradient of a scalar can have only a finite $m=1$ component and likewise the divergence of a vector can have only a finite $m=0$ component at the origin. Repeated application of these operations leads to the above result.) Using these facts, we can derive evolutionary equations for the Fourier coefficients to be advanced at the origin by taking the limit of (4a)–(4h) as $r \to 0$. We find

$$\frac{\partial \tilde{B}_{r_1}}{\partial t} = \tilde{v}_{r_1}\left(\frac{\partial \tilde{B}_{r_0}}{\partial r} + i\frac{\partial \tilde{B}_{\theta_0}}{\partial r}\right) - \tilde{B}_{r_1}\left(\frac{\partial \tilde{v}_{r_0}}{\partial r} + \frac{\partial \tilde{v}_{\zeta_0}}{\partial \zeta} - i\frac{\partial \tilde{v}_{\theta_0}}{\partial r}\right)$$
$$- \tilde{v}_{\zeta_0}\frac{\partial \tilde{B}_{r_1}}{\partial \zeta} + \tilde{B}_{\zeta_0}\frac{\partial \tilde{v}_{r_1}}{\partial \zeta} - \alpha\varepsilon\tilde{B}_{r_1}(\tilde{v}_{r_1} + \tilde{v}_{r_{-1}}) + \eta_0\left\{2\frac{\partial^2 \tilde{B}_{r_1}}{\partial r^2}\right.$$
$$\left. + \frac{\partial^2 \tilde{B}_{r_1}}{\partial \zeta^2} + \frac{\alpha\varepsilon}{2}\left[\frac{\partial \tilde{B}_{r_0}}{\partial r} - \varepsilon\left(\tilde{B}_{r_1} + \tilde{B}_{r_{-1}} - 2\frac{\partial \tilde{B}_{\zeta_0}}{\partial \zeta}\right)\right]\right\}, \tag{32a}$$

$$\frac{\partial \tilde{B}_{\zeta_0}}{\partial t} = -2\left(\tilde{v}_{r_1}\frac{\partial \tilde{B}_{\zeta_{-1}}}{\partial r} + \tilde{v}_{r_{-1}}\frac{\partial \tilde{B}_{\zeta_1}}{\partial r}\right) + 2\left(\tilde{B}r_1\frac{\partial \tilde{v}_{\zeta_{-1}}}{\partial r} + \tilde{B}_{r_{-1}}\frac{\partial \tilde{v}_{\zeta_1}}{\partial r}\right)$$
$$- 2\tilde{B}_{\zeta_0}\frac{\partial \tilde{v}_{r_0}}{\partial r} - \tilde{v}_{\zeta_0}\frac{\partial \tilde{B}_{\zeta_0}}{\partial \zeta} - \alpha\varepsilon\left[\tilde{v}_{\zeta_0}\left(\tilde{B}_{r_1} + \tilde{B}_{r_{-1}}\right) - \tilde{v}_{\zeta_0}\frac{\partial \tilde{B}_{\zeta_0}}{\partial \zeta}\right]$$
$$+ \eta_0\left\{2\frac{\partial^2 \tilde{B}_{\zeta_0}}{\partial^2 r} + \frac{\partial^2 \tilde{B}_{\zeta_0}}{\partial^2 \zeta} + \alpha\varepsilon\left[\frac{\partial \tilde{B}_{\zeta_1}}{\partial r} + \frac{\partial \tilde{B}_{\zeta_{-1}}}{\partial r}\right.\right.$$
$$\left.\left. - 2\varepsilon\left(\frac{\tilde{B}_{\zeta_0}}{2} - \frac{\partial \tilde{B}_{r_1}}{\partial \zeta} - \frac{\partial \tilde{B}_{r_{-1}}}{\partial \zeta}\right)\right]\right\}, \tag{32b}$$

$$\frac{\partial \tilde{v}_{r_1}}{\partial t} = -\tilde{v}_{r_1}\frac{\partial \tilde{v}_{r_0}}{\partial r} - \tilde{v}_{\zeta_0}\frac{\partial \tilde{v}_{r_1}}{\partial \zeta} + \frac{1}{\tilde{\rho}_0}\left[\tilde{B}_{\zeta_0}\left(\frac{\partial \tilde{B}_{r_1}}{\partial \zeta} - \frac{\partial \tilde{B}_{\zeta_1}}{\partial r}\right)\right.$$
$$\left. - i\tilde{B}_{r_1}\frac{\partial \tilde{B}_{\theta_0}}{\partial r}\right] - \frac{1}{2\rho_0}\frac{\partial \tilde{p}_1}{\partial r} + \frac{\alpha\varepsilon}{2}\left(\tilde{v}_{\zeta_0}^2 - \frac{1}{\tilde{\rho}_0}\tilde{B}_{\zeta_0}^2\right), \tag{32c}$$

$$\frac{\partial \tilde{v}_{\zeta_0}}{\partial t} = -2\left(\tilde{v}_{r_1}\frac{\partial \tilde{v}_{\zeta_{-1}}}{\partial_r} + \tilde{v}_{r_{-1}}\frac{\partial \tilde{v}_{\zeta_1}}{\partial r}\right) - \tilde{v}_{\zeta_0}\frac{\partial \tilde{v}_{\zeta_0}}{\partial \zeta} - \frac{1}{2\tilde{\rho}_0}\frac{\partial \tilde{p}_0}{\partial \zeta}$$
$$+ \frac{2}{\tilde{\rho}_0}\left[\tilde{B}_{r_1}\left(\frac{\partial \tilde{B}_{\zeta_{-1}}}{\partial r} - \frac{\partial \tilde{B}_{r_{-1}}}{\partial \zeta}\right) + \tilde{B}_{r_{-1}}\left(\frac{\partial \tilde{B}_{\zeta_1}}{\partial r} - \frac{\partial \tilde{B}_{r_1}}{\partial \zeta}\right)\right]$$
$$+ \alpha\varepsilon\left[\frac{\tilde{B}_{\zeta_0}}{\tilde{\rho}_0}(\tilde{B}_{r_1} + \tilde{B}_{r-1}) - \tilde{V}_{\zeta_0}(\tilde{v}_{\zeta_1} + \tilde{v}_{\zeta_{-1}})\right], \tag{32d}$$

$$\frac{\partial \tilde{\rho}_0}{\partial t} = -2\left(\tilde{v}_{r_1}\frac{\partial \tilde{\rho}_{-1}}{\partial r} + \tilde{v}_{r_{-1}}\frac{\partial \tilde{\rho}_1}{\partial r}\right) - \tilde{\rho}_0\left(2\frac{\partial \tilde{v}_{r_0}}{\partial r} + \frac{\partial \tilde{v}_{\zeta_0}}{\partial \zeta}\right)$$

$$- \tilde{v}_{\zeta_0}\frac{\partial \tilde{\rho}_0}{\partial \zeta} + \alpha\varepsilon\tilde{\rho}_0(\tilde{v}_{r_1} + \tilde{v}_{r_{-1}}), \tag{32e}$$

where $\tilde{u}_m$ denotes the mth complex Fourier coefficient of the variable u.

In Eqs. (32a)–(32e) the first derivative with respect to radius of the $m = 0$ components of vectors and the $m = 1$ components of scalars at $r = 0$ is evaluated by simply finding the amplitude of these quantities at the first radial mesh point and dividing by Δr. Likewise, the second derivative with respect to radius of the $m = 1$ components of vectors and the $m = 0$ components of scalars at $r = 0$ is evaluated by subtracting the values of these quantities at the first mesh point from those at the origin and multiplying by $2/\Delta r^2$.

4. Temporal Approximation

4.1. *Splitting of Spatial Operators*

We can write Eqs. (4a)–(4h) symbolically as

$$\frac{\partial \mathbf{U}}{\partial t} = \mathbf{D}_1 \cdot \mathbf{U} + \mathbf{D}_2 \cdot \mathbf{U}, \tag{33}$$

where $\mathbf{U} = (\mathbf{B}, \mathbf{V}, \rho, p)$ is the solution vector, and the operators $\mathbf{D}_1$ and $\mathbf{D}_2$ represent the first- and second-order derivatives, respectively. Examination of equations (4a)–(4h) shows that the first-order operator $\mathbf{D}_1$ can be written as

$$\mathbf{D}_1 = \mathbf{R} + \boldsymbol{\Theta} + \mathbf{Z}, \tag{34}$$

where $\mathbf{R}$, $\boldsymbol{\Theta}$, and $\mathbf{Z}$ contain only radial, poloidal, and toroidal spatial derivatives, respectively. We make use of this splitting in the time-advancement algorithm, discussed below.

4.2. *Adjective Terms: Leapfrog*

The form of Eq. (34) suggests the successive application of the formulas

$$\frac{\mathbf{U}^{(1)} - \mathbf{U}^{n-1}}{\Delta t} = \mathbf{R}_{\mathrm{FD}} \cdot \mathbf{U}^n, \tag{35a}$$

$$\frac{\mathbf{U}^{(2)} - \mathbf{U}^{(1)}}{\Delta t} = \boldsymbol{\Theta}_{\mathrm{PS}} \cdot \mathbf{U}^n, \tag{35b}$$

$$\frac{\hat{\mathbf{U}} - \mathbf{U}^{(2)}}{\Delta t} = \mathbf{Z}_{\mathrm{PS}} \cdot \mathbf{U}^n, \tag{35c}$$

where $\Delta t = t^{n-1} - t^{n-1}$, $\mathbf{U}^{n-1} = \mathbf{U}(t^{n-1})$, $\mathbf{U}^n = \mathbf{U}(t^n)$, and $\mathbf{U}^{(1)}$, $\mathbf{U}^{(2)}$, and $\hat{\mathbf{U}}$ are successive approximations to $\mathbf{U}^{n+1} = \mathbf{U}(t^{n+1})$. The subscripts FD and PS refer to the finite difference and pseudospectral approximations to the differential operators, as discussed in Section 2.

The representation (35) allows each spatial coordinate to be treated individually. This effectively separates the finite difference and pseudospectral operators. It results in reduced storage requirements, and allows each dimension to individually take advantage of machine hardware features, in particular vectorization.

Since the time integrations are performed explicitly the operations indicated by Eqs. (35a)–(35c) commute. Therefore the difficulties that can arise due to the requirement that each individual split step be a mathematically well-posed problem in the case where each step is calculated implicitly (a nonlinear finite approximation requires iteration to convergence) do not occur [24].

If one assumes $\eta = \eta_0(r)$, then the terms in Eqs. (1a)–(1d) proportional to $\nabla\eta$ can also be written in the form (34). Even though they strictly arise from the same term as the diffusion operator, they are included in this step of the algorithm because they are of lower order and hence have little effect on stability [25].

In addition to the leapfrog algorithm (35a)–(35c), we employ an averaging technique that replaces the solution $\mathbf{U}^n$ by the average of $\mathbf{U}^{n+1}$ and $\mathbf{U}^{n-1}$. We have found that the application of this averaging every 100 time steps is sufficient to avoid the decoupling instability that is inherent in the leapfrog scheme.

4.3. *Time Step Restriction*

A straightforward stability analysis of model equations of the form (35), with r approximated by finite differences, and θ and ζ by pseudospectral methods, leads to a restriction on the time step

$$\Delta t \leqslant \frac{2}{\left| \dfrac{a_r}{\Delta r} + \dfrac{M a_\theta}{r} + N\varepsilon a_\zeta \right|}, \tag{36}$$

where $M = N_\theta/2$ is the largest poloidal mode number, $N = N_\zeta/2$ is the largest toroidal mode number, and $a_\alpha(\alpha = r, \theta, \zeta)$ is given by

$$a_\alpha = |v_\alpha| + \sqrt{c_s^2 + v_A^2}, \tag{37}$$

where $c_s^2 = \gamma p/\rho$ is the square of the local sound speed and $v_A^2 = B^2/\rho$ is the square of the local Alfvén speed.

Since $M \sim 1/\Delta\theta$, Eq. (36) can be quite restrictive near the origin ($r = 0$), becoming formally second order for $r \sim \Delta r$. The source of this problem is that the poloidal mesh, while uniform in $\Delta\theta$, is nonuniform in arc length $\Delta s = r\Delta\theta$. The mesh thus

allows for much shorter wavelengths to be resolved near the origin than near the outer boundary. The problem is alleviated by replacing the fixed number M by a function $M(r) \leqslant M$ such that wavelengths shorter than those resolvable near the boundary ($\lambda_a = 2a\Delta\theta$) are removed from the calculation [26]. This smoothing, or filtering, of poloidal modes as a function of radius restores Eq. (36) to first order with a considerable gain in allowable time step.

Theoretically, the filtering procedure described above allows only modes with poloidal mode number $m = 0$ to exist near to $r = 0$. In order to accurately model the dynamics, clearly $m = 1$ must also be allowed. We have found that for many cases this is also too restrictive, and accurate results are obtained by allowing $m = 2$ to extend to $r = 0$.

4.4. *Diffusion Terms: Implicit*

The time step restriction (36) applies only to the advective terms discussed in the previous section. When diffusive terms arising from second-order spatial operations are considered, the time step restriction is formally second order everywhere. When η_0 is small enough (the cell Reynolds number $R_\Delta = v\Delta r/\eta_0 > 1$), the advective time step restriction dominates. However, in cases where $\eta_0(r)$ has large spatial variation the diffusive restriction may dominate locally. To circumvent this problem we advance the diffusive terms (terms proportional to η_0) in Eqs. (4a)–(4h) by the implicit algorithm

$$[1 - \eta_0 w \Delta t L^2_{m,l}]\, \tilde{\mathbf{B}}^{n+1}_{m,l} = \eta_0(1 - w)\, \Delta t L^2_{m,l} \tilde{\mathbf{B}}^{n-1}_{m,l} + \hat{\mathbf{B}}_{m,l}, \tag{38}$$

where $\tilde{\mathbf{B}}^{n\pm1}_{m,l}(r)$ is the (m, l) complex Fourier coefficient of $\mathbf{B}(\mathbf{r}, t^{n+1})$, $\hat{\mathbf{B}}_{m,l}(r)$ is the (m, l) complex Fourier coefficient of the advective approximation to $\mathbf{B}(\mathbf{r}, t^{n+1})$ [obtained from Eq. (35c)], $L^2_{m,l}$ is the spectral-finite difference approximation to the Laplacian, and w is a coefficient such that $(0 \leqslant w \leqslant 1)$. When $w \geqslant 0.5$ the algorithm is unconditionally stable, and when $w = 0.5$ it is second-order accurate in Δt. The three-point operator on the left-hand side of Eq. (38) is easily inverted using the well-known tridiagonal algorithm [25].

5. Examples

In this section we briefly describe several examples of applications of the algorithms presented here. These problems are all relevant to simulation of the reversed field pinch (RFP), a diffuse toroidal pinch with toroidal and poloidal magnetic field of comparable magnitude. The model presented in this paper is thus appropriate, for reasons discussed in Section 2.

5.1. *Toroidal Equilibrium*

Magnetohydrodynamic equilibrium is defined by the force balance condition

$$\nabla p = \mathbf{J} \times \mathbf{B}, \tag{39}$$

which is the steady-state, zero flow limit of Eq. (1b). For a straight cylindrical system, solutions of (39) are functions of r only. These solutions are characterized by circular concentric surfaces centered at $r = 0$.

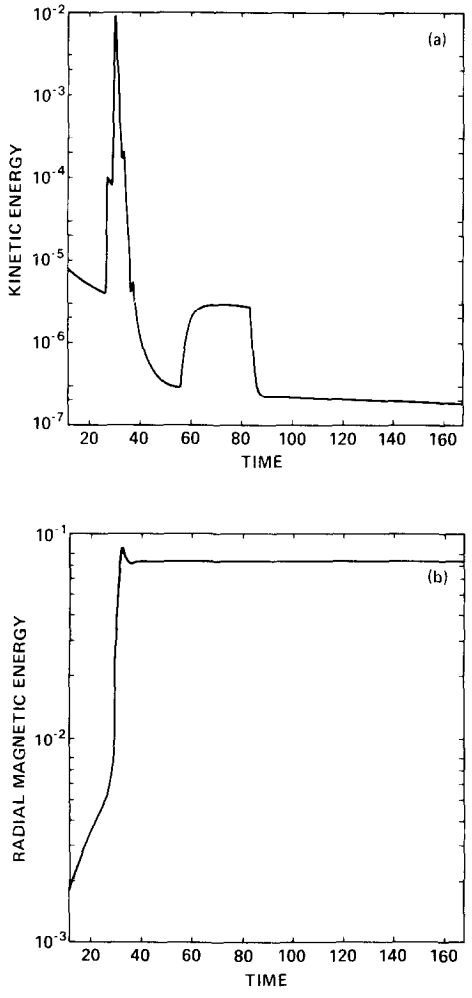

FIG. 2. (a) Kinetic energy versus time for relaxation to toroidal equilibrium. The nonuniform behavior is the result of the application of different values of the friction parameter ν throughout the calculation. (b) Energy in the radial component of the magnetic field versus time for the toroidal relaxation shown in (a).

When toroidal effects are introduced axisymmetric (ζ-independent) solutions are functions of both r and θ. The accurate numerical solution of these problems has been the topic of much research [27]. However, in many instances (such as obtaining initial conditions for dynamical simulations) such accurate methods are not required, and toroidal equilibria may be obtained by dynamical relaxation. In this method the initial conditions consist of a known cylindrical equilibrium. Of course, this solution does not represent equilibrium in a torus, and as time proceeds the nondissipative dynamical equations cause flows to appear that move the plasma toward a state of force balance. Because of the kinetic energy of the flow, the system will overshoot its new equilibrium position resulting in oscillations that may continue indefinitely, unless damped. This is accomplished by rewriting Eq. (1b) as

$$\frac{d\mathbf{v}}{dt} = \mathbf{F} - \nu\mathbf{v}, \tag{40}$$

where the left-hand side represents the advective derivative, $\mathbf{F}$ is the combined pressure and Lorentz forces, and ν is a friction coefficient chosen to remove the kinetic energy from the system. When the kinetic energy becomes less than some prescribed value, a toroidal equilibrium has been determined.

In Figs 2a, b we show the kinetic and radial magnetic energies as a function of time for such a calculation. The initial (cylindrical) state is characterized by profile of the form

$$q(r) = q_0(1 + ar^2 + br^4), \tag{41}$$

where $q = \varepsilon r B_\zeta / B_\theta$ is called the safety factor, $q_0 = q(0)$, an a and b are constants. For the configuration considered, we have $\varepsilon = 0.2$, $q(0) = 0.1$. In general, a pressure profile $p(r)$ must also be specified. For this case, and all subsequent examples in this paper, we have taken $p = 0$ initially. Then Eqs. (39) and (41) completely specify the cylindrical solution. We see in Fig. 2 that the plasma approaches toroidal equilibrium. The nonuniform behavior of the kinetic energy is the result of the application of different values of ν throughout the calculation.

The axisymmetric flux surfaces in the initial and final states are shown in Figs. 3a, b. These are the level curves of the function $\psi(r, \theta)$ defined by

$$\frac{\partial \psi}{\partial r} = -\frac{1}{\tau} B_\theta, \qquad \frac{\partial \psi}{\partial \theta} = \frac{r}{\tau} B_r, \tag{42a, b}$$

where τ is defined in Eq. (3c). We see that in the resulting toroidal equilibrium, the flux surfaces are no longer concentric circles, and that the magnetic axis (the point where $B_\theta = 0$) has shifted slightly outward a distance $\delta r/a \approx 0.05$. This shift is small, in agreement with theory [28].

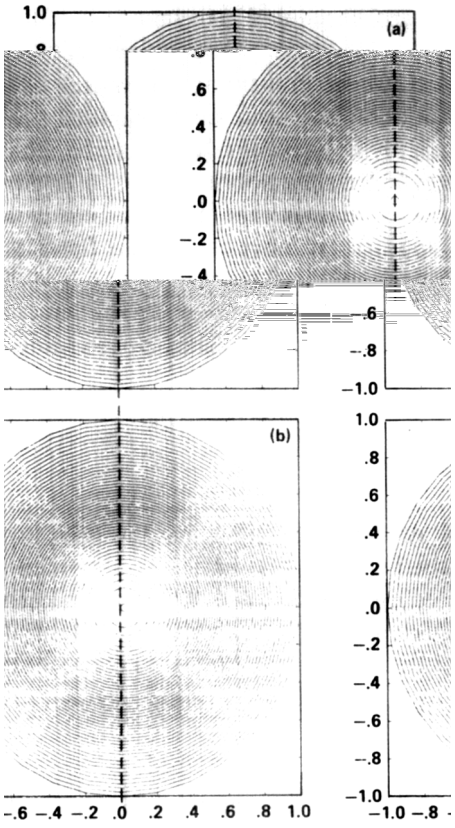

FIG. 3. Initial (a) and final (b) flux surfaces for the toroidal relaxation problem. Note the slight toroidal shift characteristic of the reversed field pinch.

5.2. *Helically Symmetric Simulations*

Because of the slight nature of the toroidal shift in RFP configurations, it is sufficient in many cases to carry out calculations in cylindrical geometry. Then the dynamical Eqs. (4a)–(4h) preserve helical symmetry. Thus if initial conditions are prescribed by a given helicity $h = n/m$, where n and m are axial (toroidal) and poloidal mode numbers, then all modes (m, n) generated nonlinearly will retain the same helicity h. This property of the MHD equations has been exploited previously to allow the solution of certain three-dimensional problems with two-dimensional codes [1, 3], and has yielded valuable insight into plasma dynamics. In our case such problems may be reproduced, as the numerical solution described in this paper also preserves initial helicity exactly.

In Figs. 4a–f we show the helical flux surfaces at various times resulting from the nonlinear evolution of the $m = 1$, $n\varepsilon = 0.3$ tearing instability in the force-free Bessel function equilibrium

$$B_\theta(r) = J_1(r), \tag{43a}$$

$$B_z(r) = J_0(r), \tag{43b}$$

which is a cylindrically symmetric solution of (39) when $p = 0$. These flux surfaces are level curves of the helical flux function

$$\Psi_h(r, \theta) = \int_a^r [b_{\theta_{0,0}}(r') + r' h \in b_{z_{0,0}}(r')]\, dr'$$

$$- \frac{ir}{m} b_{r_{m,n}}(r)\, e^{im\theta} + \text{c.c.}, \tag{44}$$

where $h = n/m$ is the helicity, $b_{r_{m,n}}$, $b_{\theta_{m,n}}$, and $b_{z_{m,n}}$ are the (m, n) complex Fourier

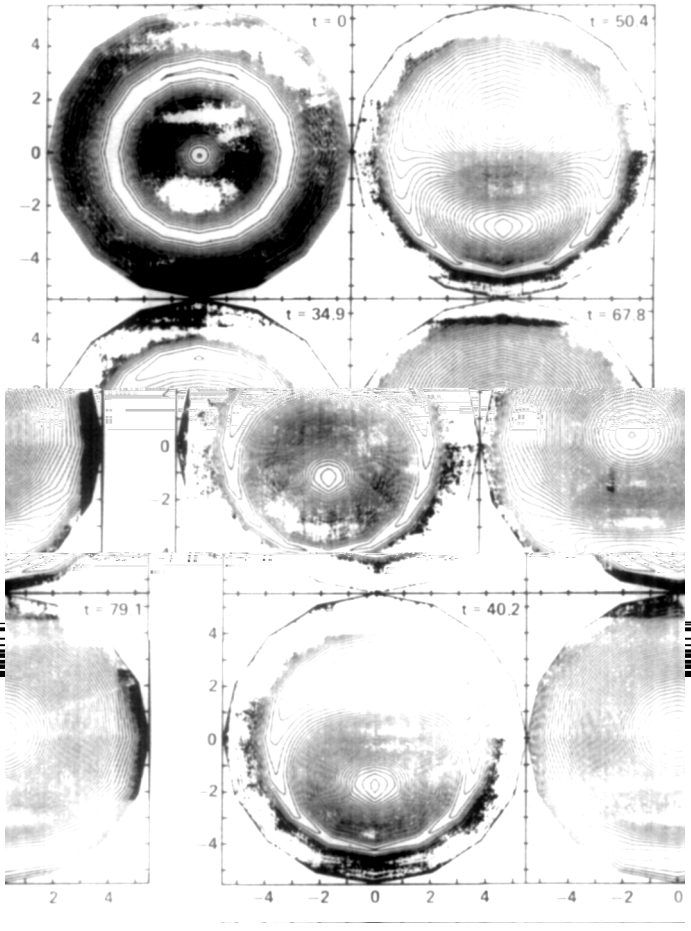

FIG. 4. Helical flux surfaces at various times for the nonlinear evolution of the $m = 1$, $n\varepsilon = 0.3$ tearing mode in the Bessel function model equilibrium.

coefficients of the magnetic fields, and c.c. denotes complex conjugate. In helical symmetry the magnetic field lines are tangent to these contours. Figure 4 is in close agreement with previous two-dimensional helical results [3, 5].

5.3. *Mode Interaction*

Fully three-dimensional effects are observed when the initial conditions contain more than one helicity. In this cylindrical example, the initial conditions consist of the force-free equilibrium (41) with $q_0 = 0.15748$, $a = -1.8748$, $b = 0.8323$, along with the two linearly unstable eigenmodes ($m = 1$, $n = -10$) and ($m = 1$, $n = -11$).

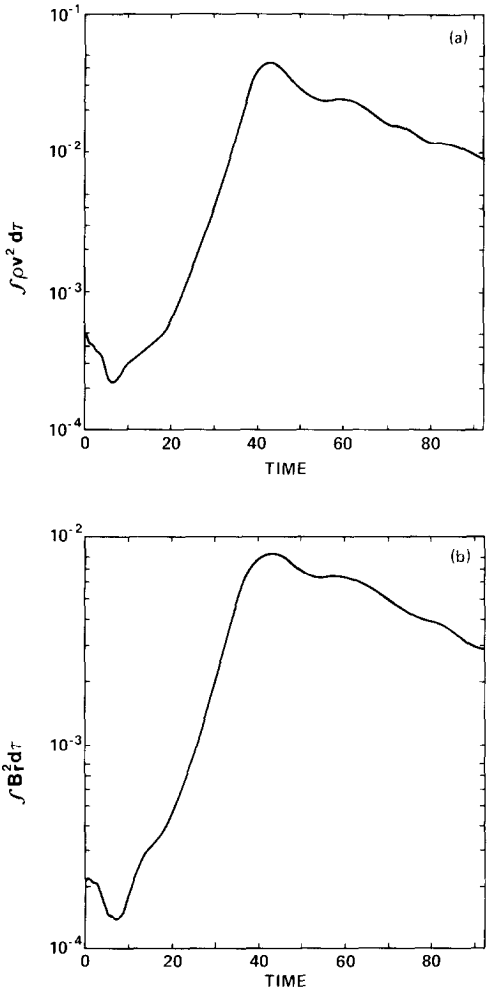

FIG. 5. Kinetic (a) and radial magnetic (b) energies versus time for a three-dimensional simulation.

These modes are obtained from a linear resistive MHD code that employs the method of matrix shooting [29]. The $(m = 1, n = -10)$ mode in this equilibrium has been the focus of detailed single helicity calculations [7].

The case is run on a grid of 65 radial mesh points, 8 poloidal mesh points (modes), and 64 axial mesh points (modes). This allows for the higher harmonics $(2, -20)$, $(2, -21)$, and $(2, -22)$ resulting from mode interaction to be well represented in the calculation. The accurate computation of all 512 modes and their interaction would be impractical without the fast transform techniques presented in this paper.

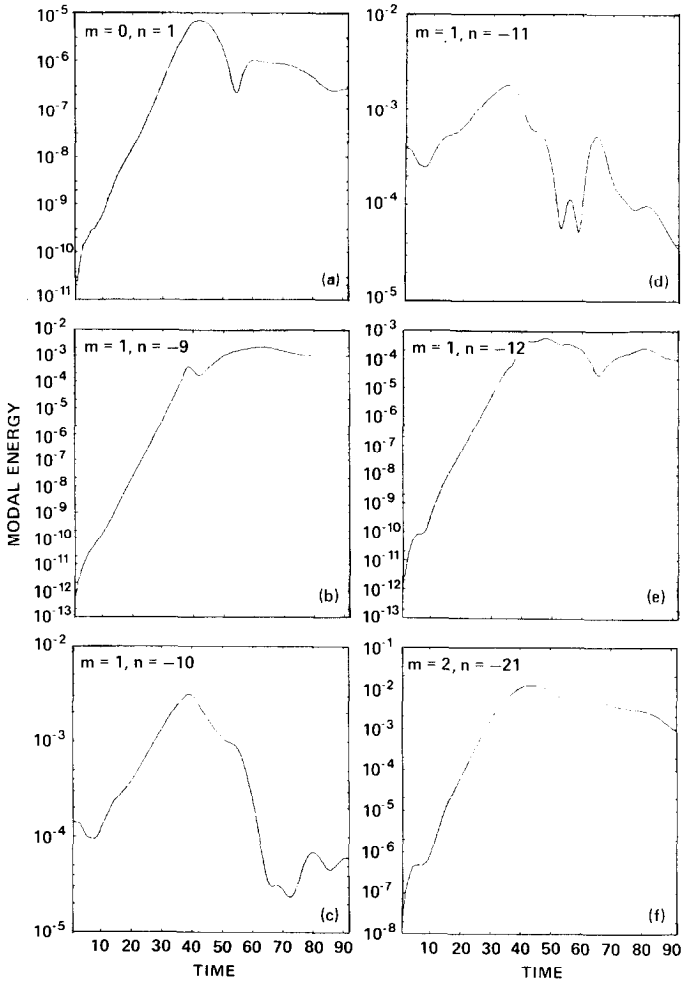

FIG. 6. Energy $E_{m,n}$ in various (m, n) modes for the three-dimensional case of Fig. 5. The initial conditions consisted of $(0, 0)$, $(1, -10)$, and $(1, -11)$ only. Many more modes are present than shown here.

In Fig. 5 we plot the kinetic and radial magnetic energies

$$E_k = \int \rho v^2 \, d^3\mathbf{r}, \qquad E_r = \int B_r^2 \, d^3\mathbf{r} \tag{45}$$

as functions of time for this case. We see a period of exponential growth followed by nonlinear saturation and relaxation for $t \geqslant 40 t_A$. In Fig. 6 we plot the energy in various (m, n) modes

$$E_{m,n} = \int_0^a b^*_{r_{m,n}}(r)\, b_{r_{m,n}}(r) r \, dr, \tag{46}$$

where $b_{r_{m,n}}$ is the complex Fourier coefficient of B_r, as function of time. Note that many unstable modes appear in addition to those initialized at $t = 0$.

In Fig. 7 we plot the helical flux contours [Eq. (44)] for several (m, n) modes in the system at various times. It is seen that this configuration is rich is model activity. Note that in three dimensions these contours merely aid in visualization, and have no relation to magnetic field lines as they do in the case of single helicity.

In Fig. 8 we plot the spectral energy, Eq. (46), for $m = 0$, 1, and 2 as a function of

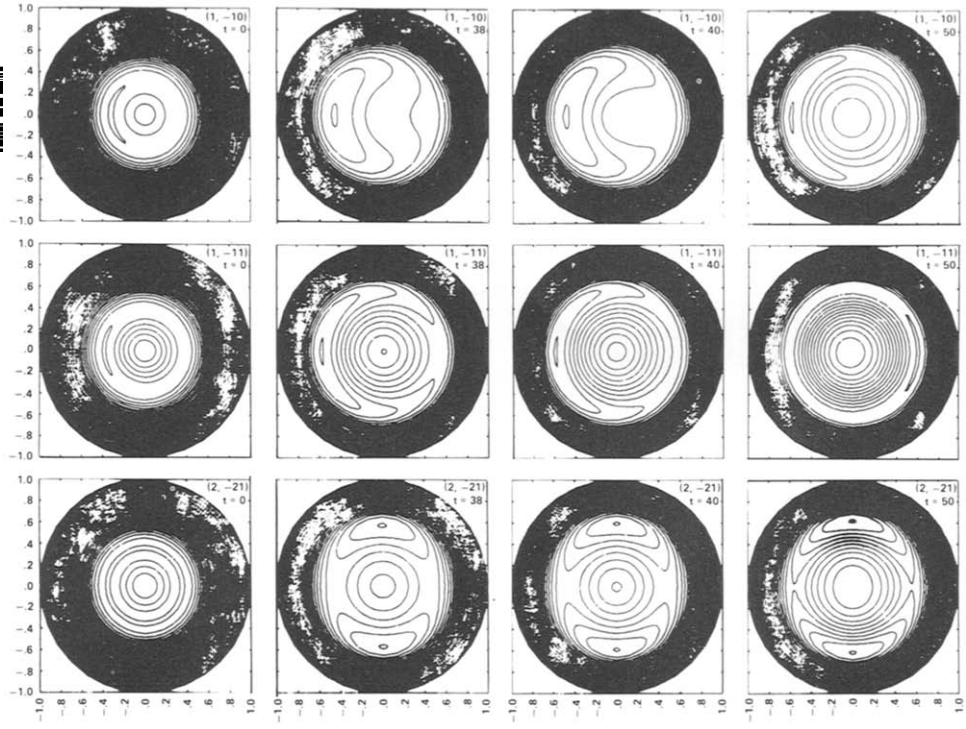

FIG. 7. Helical flux contours for several (m, n) modes in the three-dimensional simulation.

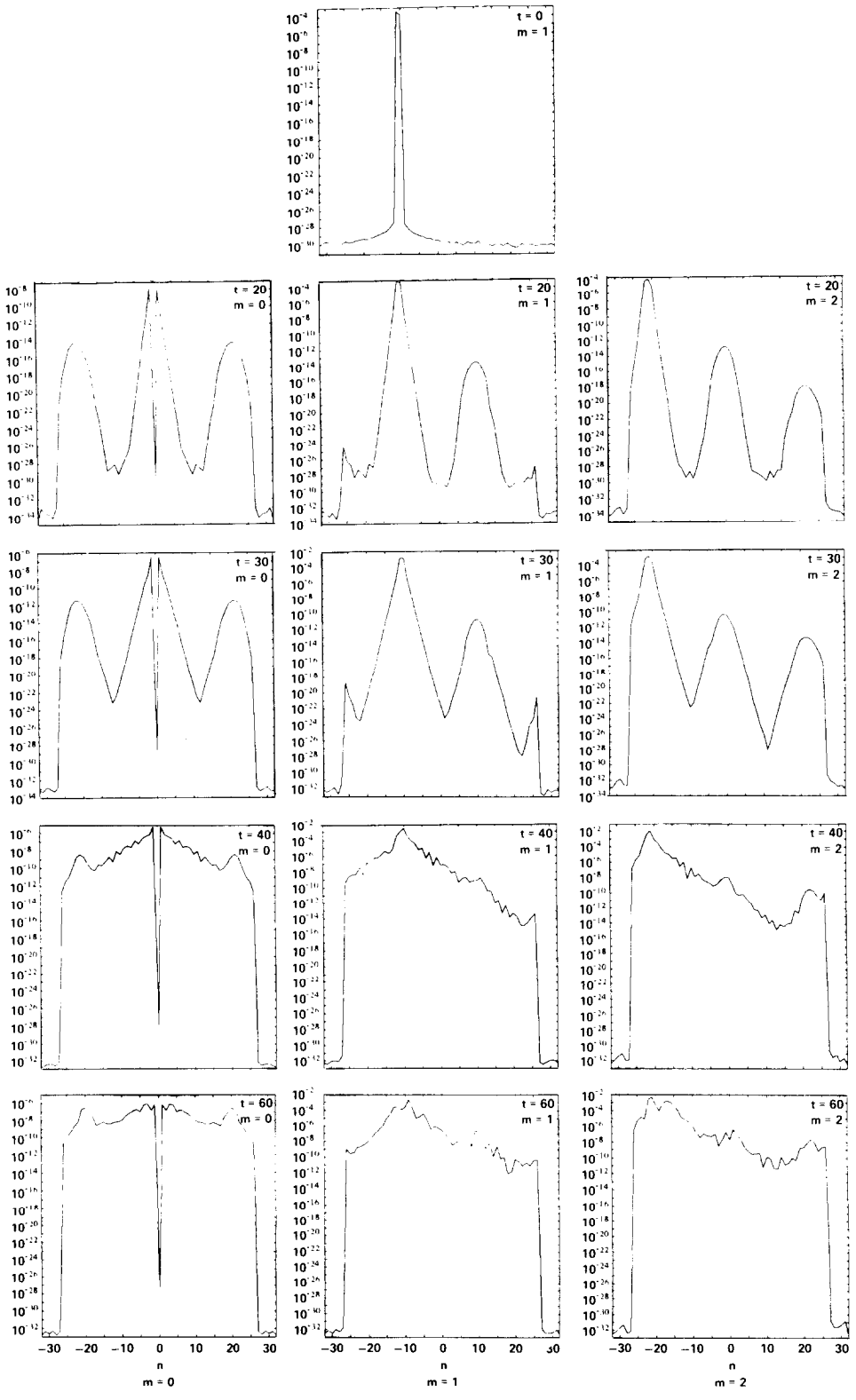

FIG. 8. Energy $E_{m,n}$ for $m = 0, 1$, and 2 as functions of n at various times during the three-dimensional simulation.

n a various times. The sharp cutoff at large $|n|$ is due to dealising, as discussed in Section 3.2.1. Note the broadening of the spectrum about the initial $(1, -10)$ and $(1, -11)$ modes, and the early generation of modes with opposite helicity $h = n/m$. The spectrum is fully developed by the saturation time $t = 40\, t_A$. It is difficult if not impossible to select preferential modes in this case. Such turbulent states are most accurately modeled by the spectral methods presented here. This and similar cases will be discussed in more detail in a future publication.

5.4 *Comparison with Finite Differences*

In this section we compare the results of the pseudospectral algorithm with those obtained by finite differences. For our algorithm this is a relatively simple matter, as all derivative arrays are calculated in subroutines. The choice of finite differences or spectral computation is simply controlled by a switch in the routine.

For a comparison we choose Eq. (45) and its growth rate

$$\gamma_{N_s}(t) = \frac{1}{2E_r}\frac{dE_r}{dt}, \tag{47}$$

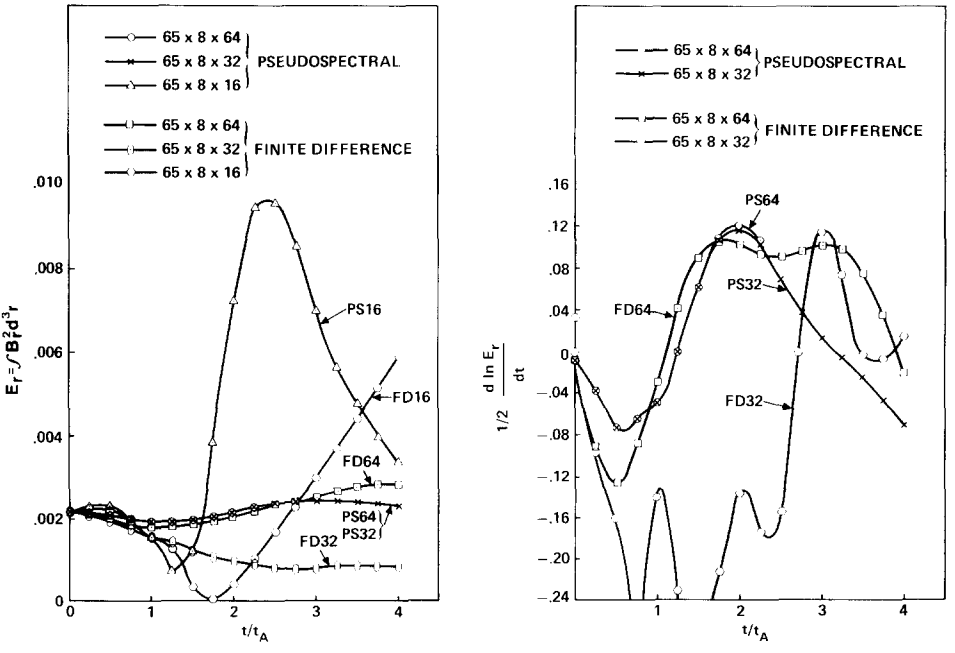

FIG. 9. (a) Radial magnetic energy versus time for several axial mesh sizes for both pseudospectral (PS) and finite difference (FD) calculations. Note that PS64 and PS32 are indistinguishable from another. (b) Growth rate of the curves shown in (a). Note the poorer convergence properties of finite difference methods.

for both finite differences and the pseudospectral algorithm for various values of the number of axial mesh points (modes) N_ζ.

The results are summarized in Figs. 9a, b, where we plot E_r and γ versus t for both methods for various axial meshes. When $N_\zeta = 64$ (the base case) the two methods are in substantial agreement. When $N_\zeta = 32$ the results begin to diverge, with the pseudospectral results closely following the base. When $N_\zeta = 16$ neither method is very accurate, but the pseudospectral method exhibits much more integrity than do finite differences.

For the same number of mesh points (modes), finite differences require somewhat less computer time than does the pseudospectral method. However, as discussed in Section 3.1.2 and demonstrated in Fig. 9, the pseudospectral method requires fewer modes to obtain comparable accuracy. We have found that, for the cases considered, the pseudospectral method requires approximately half the computer time of finite differences to obtain a given standard of accuracy.

6. Conclusions

We have developed an algorithm for the solution of the compressible, resistive MHD equations in three space dimensions. These equations are cast in local cylindrical coordinates, which can represent a circular cross-section torus or a periodic cylinder. We have approximated the radial terms by finite differences, and have used the pseudospectral algorithm for the periodic directions. We have shown that this technique, which has been extensively used in hydrodynamics, is well suited to the computation of nonlinear states of plasmas in magnetic fusion experiments when many mode interactions are involved. We have computed the turbulent states that result from the nonlinear interaction of unstable modes of different helicity. We have found that when fast transform techniques are used the pseudospectral algorithm is more efficient than finite differences in that results of comparable accuracy are obtained with less computer time.

Acknowledgments

The authors have benefited from discussions with many individuals throughout the course of this work. In particular, we wish to acknowledge Drs. A. Aydemir, D. Barnes, D. Dobrott, J. Hyman, R. Malone, W. Matthaeus, A. Mirin, D. Montgomery, R. Nebel, S. Orszag, H. Rose, and L. Turner for valuable suggestions and discussions concerning both computational and physical issues. We are particularly indebted to W. Matthaeus for supplying the software described in Ref. [23]. This work was performed under the auspices of the U.S. Department of Energy, in part under Subcontract 9-X13-4935W-1 with Los Alamos National Laboratory and in part under Contract DE-AC03-83ER53150.

REFERENCES

1. B. V. WADDELL, M. N. ROSENBLUTH, D. A. MONTICELLO, AND R. B. WHITE, *Nucleon Fusion* **16** (1976), 528.
2. B. CARRERAS, B. V. WADDELL, H. R. HICKS, AND S. J. LYNCH, *Phys. Rev. A* **18** (1978), 735.
3. D. SCHNACK AND J. KILLEEN, *J. Comput. Phys.* **35** (1980), 110.
4. G. L. JAHNS, M. SOLER, B. V. WADDELL, J. D. CALLEN, AND H. R. HICKS, *Nuclear Fusion* **18** (1978), 609.
5. D. SCHNACK AND J. KILLEEN, *Nuclear Fusion* **19** (1979), 877.
6. D. D. SCHNACK, J. KILLEEN, AND R. A. GERWIN, *Nuclear Fusion* **21** (1981), 447.
7. E. J. CARAMANA, R. A. NEBEL, AND D. D. SCHNACK, *Phys. Fluids* **26** (1983), 1305.
8. B. V. WADDELL, B. CARRERAS, H. R. HICKS, AND J. A. HOLMES, *Phys. Fluids* **22** (1979), 896.
9. B. CARRERAS, H. R. HICKS, J. A. HOLMES, AND B. WADDELL, *Phys. Fluids* **23** (1980), 1811.
10. H. STRAUSS, *Phys. Fluids* **19** (1976), 134.
11. B. CARRERAS, H. R. HICKS AND D. K. LEE, *Phys. Fluids* **24** (1981), 66.
12. A. Y. AYDEMIR AND D. C. BARNES, *J. Comput. Phys.* **54** (1984), 100.
13. B. A. CARRERAS, M. N. ROSENBLUTH, AND H. R. HICKS, *Phys Rev. Lett.* **46**, (1981), 1131.
14. H. R. HICKS, B. A. CARRERAS, J. A. HOLMES, D. K. LEE, AND B. V. WADDELL, *J. Comput. Phys.* **44** (1981), 46.
15. S. A. ORSZAG, *Stud. Appl. Math.* **50** (1971), 293.
16. S. A. ORSZAG, *J. Fluid Mech.* **49** (1971), 75.
17. S. A. ORSZAG, *Stud. Appl. Math.* **51** (1972), 253.
18. G. S. PATTERSON, JR., AND S. A. ORSZAG, *Phys. Fluids* **14** (1971), 2538.
19. D. G. FOX AND S. A. ORSZAG, *J. Comput. Phys.* **11** (1973), 612.
20. D. GOTTLIEB AND S. A. ORSZAG, "Numerical Analysis of Spectral Methods: Theory and Applications," SIAM, Philadelphia, 1977.
21. S. I. BRAGINSKII, *in* "Reviews of Plasma Physics" (M. A. Leontovitch, Ed.), Vol. 1, Sect. 6, p. 262, Consultants Bureau, New York, 1965.
22. H. P. FURTH, J. KILLEEN, AND M. N. ROSENBLUTH, *Phys. Fluids* **6** (1963), 459.
23. C. TEMPERTON, *Comput. Phys. Comm.* **26** (1982), 331.
24. A. R. MITCHELL, "Computational Methods in Partial Differential Equations," Wiley, London/New York, 1969.
25. R. D. RICHTMEYER AND K. W. MORTON, "Difference Methods for Initial Value of Problems," 2nd ed., Interscience, New York, 1967.
26. S. A. ORSZAG, private communication, 1982.
27. B. MCNAMARA, *in* "Methods in Computational Physics," Vol. 16, p. 211, Academic Press, New York, 1976.
28. V. D. SHAFRANOV, *in* "Reviews of Plasma Physics," Vol. 2, p. 103, Consultants Bureau, New York, 1963.
29. J. P. FREIDBERG AND D. W. HEWETT, *J. Plasma Phys.* **26** (1981), 177.